catalysts

MDPI

Communication

Theoretical Study on the Mechanism of CO* Electrochemical Reduction on Cu(111) under Constant Potential

Shange Mei * and Wanzhen Liang

College of Chemistry and Chemical Engineering, Xiamen University, Xiamen 361005, China
* Correspondence: meishange@stu.xmu.edu.cn

Abstract: In order to understand the mechanism of the electrochemical reduction of CO* on Cu(111), which competitively generates two intermediates, CHO* and COH*, we performed a first principles calculation on these two electrocatalytic reactions, including the solvent effect and imposing a constant potential. The transition states of the two reactions under constant potential conditions were located by the electrochemical nudged elastic band (eNEB) method and the charge effect in the two reactions was elucidated by charge correction in the constant potential model and Bader charge analysis. It was found that the two reactions have different potential dependencies and involve different degrees of partial charge transfer. In addition, we confirmed that the COH* reaction pathway exists only in a certain potential range when using the implicit solvent model.

Keywords: electrocatalysis; carbon monoxide reduction; constant potential model; implicit solvent model

check for updates

Citation: Mei, S.; Liang, W. Theoretical Study on the Mechanism of CO* Electrochemical Reduction on Cu(111) under Constant Potential. *Catalysts* **2023**, *13*, 960. https://doi.org/10.3390/catal13060960

Academic Editor: Carlo Santoro

Received: 4 April 2023
Revised: 26 May 2023
Accepted: 28 May 2023
Published: 1 June 2023

Copyright: © 2023 by the authors. Licensee MDPI, Basel, Switzerland. This article is an open access article distributed under the terms and conditions of the Creative Commons Attribution (CC BY) license (https://creativecommons.org/licenses/by/4.0/).

1. Introduction

It is a promising green chemistry strategy to recycle carbon dioxide (CO_2) in the environment and convert it into useful fuels and chemicals [1]. Electrocatalyzed CO_2 reduction, as one of the numerous converting methods, has become a research hotspot in recent years due to its advantages such as mild reaction conditions, cheap reactants, and easy control of the reaction process. Among multitudinous electrocatalysts, copper has experimentally been reported as the only pure metal catalyst that can further reduce CO molecules into hydrocarbons [2–4], possibly due to its negative adsorption energy for *CO and positive adsorption energy for surface hydrogen H* [5]. However, various reaction paths in the process of CO* reduction lead to poor reaction selectivity, thus the elucidation of the mechanism of these reactions are of great importance for the designation of highly active and selective catalysts.

Plenty of theoretical studies on the mechanism of these reactions based on experimental observations have been reported up to now. In 2010, Peterson et al. performed density functional theory (DFT) calculations on the electroreduction of CO_2 on a Cu surface and proposed a detailed reaction path including a CHO* intermediate that leads to methane production [6]. After that, in 2013, Nie et al. proposed an H-shuttling COH* path and showed that the activation barrier for the formation of COH* would be reduced by the water-assisted H-shuttling process [7]. Later in 2020, Zhao et al. re-evaluated two reaction paths involving CHO* and COH*, respectively, using embedded complete active space second-order perturbation theory (emb-CASPT2) [8]. These works showed that the first step in CO reduction is critical to the selectivity of the whole reduction process.

So far, the reported theoretical works mostly used models that contain constant charge, which may lead to an error that the surface potential of catalysts changes with the reaction process. To make the computational model closer to the reality that electrochemical reactions proceed under constant potential and undergo charge transfer from or to the electrodes, some groups developed constant potential methods [9–11]. In this work, we apply a constant-potential local minimize and saddle point search method including both

atomic positions and number of electrons as variables implemented by Duan et al. [12] to investigate the first step of CO* electroreduction on Cu(111), and the charge transfer and the solvent effect will be considered.

2. Results and Discussion

2.1. The CHO Path*

Previous calculations by Nie et al. [7] showed that water-assisted H-shuttling increases the activation barrier of forming CHO* intermediate. Therefore, we adopt the direct H* transfer mechanism in the CHO* path. We performed structural relaxation and transition state localization at potentials ranging from 0.0 V (the potential used in this work are referenced to standard hydrogen electrodes, that is, the unit V means V (vs. SHE)) to −1.6 V with steps of −0.4 V under implicit solvent and constant potential conditions. Figure 1 shows the optimized structures of the initial state (IS), transition state (TS), and final state (FS) of the CHO* path under the potential of 0.0 V.

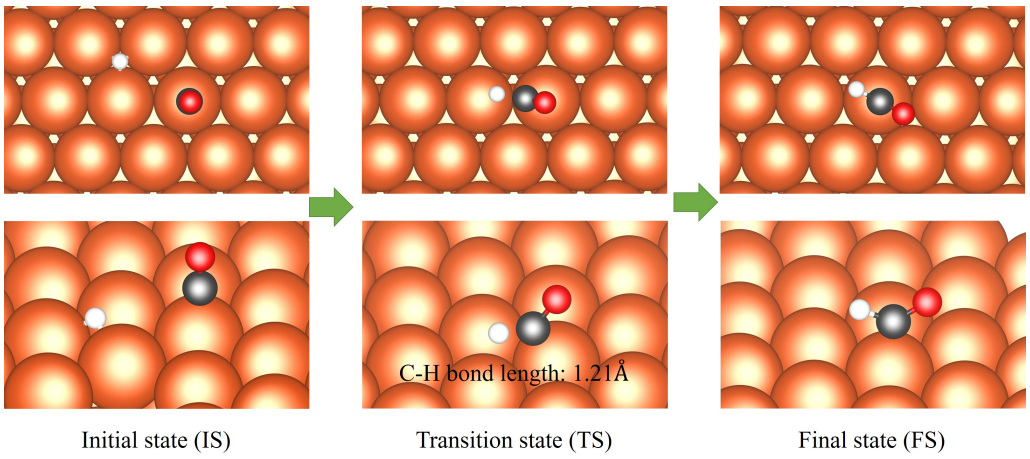

Figure 1. Top and side view of the optimized structure of IS, TS, and FS of the elementary step of CO* reduction to CHO* intermediate under the potential of 0.0 V (orange = copper, red = oxygen, grey = carbon, white = hydrogen).

We first calculated the activation barrier and reaction energy of the reaction path under each potential. It is worth noting that there exists a shallow local minimum (denoted as intermediate state, MS) close to the TS. We performed another eNEB calculation between IS and MS and found a TS, which is the same as the TS between IS and FS. Figure 2a,b show the energy changes along the minimum energy path (MEP) at each potential, where Figure 2a represents the MEP between IS and MS, and Figure 2b represents the MEP between MS and FS.

Previous studies believed that the process of CO* forming CHO* through the direct transfer of surface hydrogen is a chemical process rather than an electrochemical process [8] since no electrons transfer. That is to say, this reaction can only be written as $CO^* + H^* \longrightarrow CHO^*$ instead of $CO^* + H^+ + e^- \longrightarrow CHO^*$. Based on this, the activation energy and reaction energy of the reaction should be independent of the potential. However, our result shows that the activation energy and reaction energy of this reaction does vary with the potential, albeit to a small magnitude. The activation energies decrease from 0.84 eV at U = 0.0 V to 0.57 eV at U = −1.6 V. This is because the system charge of the IS, TS, and FS are changed to keep the potential constant (Figure 2c, dashed lines). For instance, at U = −1.2 V, the IS, TS, and FS have charges of −0.987 e, −1.196 e, and −1.170 e, respectively, which suggests that about 0.18 e charge transferred in the reaction. In addition, it can be seen from Figure 2b,c that as the applied negative potential increases, the relative stability of MS and FS changed. The energy of MS is even lower than FS at U = −1.6 V, this is the result of less changes in charge of adsorbed species.

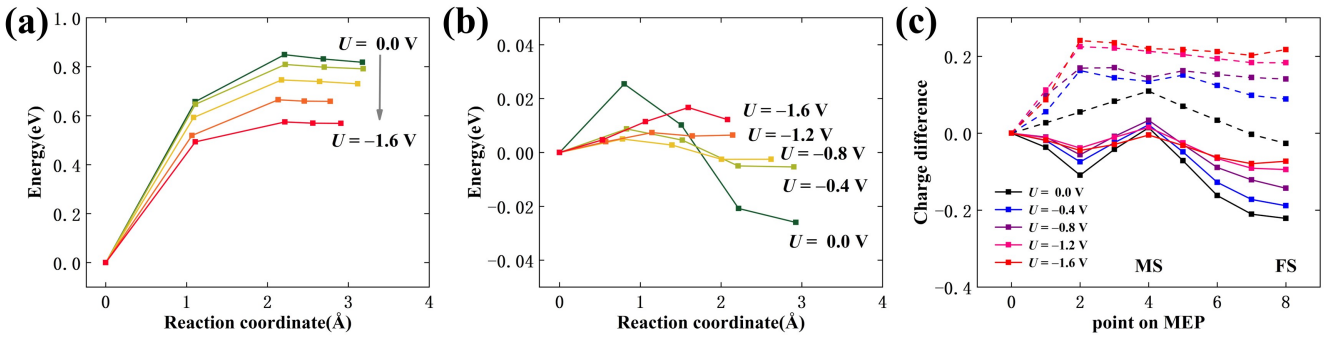

Figure 2. (**a**,**b**) Energy changes along the MEP of CO* reduction to CHO* from 0.0 V to −1.6 V, (**a**): IS to MS, (**b**): MS to FS. (**c**) Changes of system charge (dashed lines) and adsorbed species Bader charge (solid lines) along the MEP of CO* reduction to CHO* from 0.0 V to −1.6 V.

Bader charge analysis of each atom (listed in Table 1) shows that charge redistribution occurs during this process from IS to TS, and from TS to FS. Overall, with the formation of CHO*, partial charge transfer occurred from the surface species back to the copper electrode. Specifically, when the surface hydrogen H* leaves the copper surface, it returns partial charges to the copper atom, and the carbon atom absorbs partial charges from the surface and then forms a C-H bond with hydrogen. By the time CHO* is finally formed, the charge of the surface species again partially returned to the copper surface. Comparing the charge changes of carbon atoms at various potentials, we found that they all need to obtain a charge of about 0.25 e in the process from IS to TS, while the charge difference of the system between the TS and the IS increases from close to 0 to about 0.25 e as the potential becomes negative. Combined with the change in the activation barrier with the potential, we speculate that one reason for the decrease in activation energy as the potential becomes negative is that it is easier for the charged surface to donate electrons, which makes the formation of the TS easier.

Table 1. Bader charge analysis on key fragments at each point on the MEP of CHO* path at various potentials.

Potential	Atom or Fragment	Strctures along the MEP					
		IS	1	2	3	MS	FS
0.0 V	Cu [1]	0.100	0.119	0.091	0.096	0.113	0.051
	C	0.935	0.871	0.673	0.628	0.605	0.709
	O	−1.062	−1.021	−1.042	−1.039	−1.060	−1.050
	H	−0.261	−0.203	0.089	0.064	0.052	0.173
−0.4 V	Cu	0.085	0.114	0.080	0.087	0.112	0.042
	C	0.904	0.853	0.653	0.616	0.588	0.710
	O	−1.057	−1.037	−1.065	−1.063	−1.074	−1.079
	H	−0.265	−0.215	0.068	0.054	0.046	0.140
−0.8 V	Cu	0.088	0.114	0.074	0.088	0.109	0.050
	C	0.870	0.847	0.640	0.579	0.590	0.724
	O	−1.070	−1.071	−1.096	−1.081	−1.095	−1.119
	H	−0.271	−0.237	0.041	−0.039	0.001	0.067
−1.2 V	Cu	0.090	0.133	0.065	0.071	0.093	0.072
	C	0.843	0.838	0.638	0.644	0.608	0.685
	O	−1.089	−1.111	−1.127	−1.126	−1.133	−1.160
	H	−0.288	−0.250	−0.007	−0.042	−0.026	0.035

[1] Cu represents the Cu atoms whose top site is absorbed by C atom.

2.2. The COH* Path

The mechanism of *CO forming COH* intermediates through water-assisted H-shuttling was proposed by Nie et al. in 2013 [7], the subsequent steps are the formation of an additional O-H bond and then dissociating a water molecule to form a surface carbon atoms C* and then gradually hydrogenate to form methane. This reaction path can better explain the phenomenon of methane production in the CO_2 electroreduction experiment, and the participation of a water molecule also solves the problem of the high potential barrier for the formation of COH*.

When exploring the CO* to COH* mechanism using implicit solvent model, we found that the hydrogen of the final COH* intermediate could not point to the oxygen of the water molecule and be stabilized by hydrogen bonds, it would transfer back to the water molecule to form H_3O^+ species. The energy of this structure is lower than the initial state energy proposed by Nie et al. in 2013 [7] and can be regarded as the initial state of a different path. This phenomenon is similar to the situation that Nie et al. encountered in 2014 [13], they stabilized COH* by pointing the hydrogen of COH* in the opposite direction. We also tested this opposite direction COH* structure and found that it can exist in implicit solvent model. This shows that the reason why the hydrogen of COH* transferred back to the water molecule is not the instability of the O-H bond of COH* in implicit solvent model, but the energy difference between $O_w - H \cdots O_C$ and $O_w \cdots H - O_C$ hydrogen bond structure ("$\cdots$" represent a hydrogen bond, O_w represent the oxygen atom of water, and O_c represent the oxygen atom of COH*), once there is not enough energy barrier between the two structures, one will change into another structure spontaneously.

The relative energy of these two hydrogen bond structures will vary with the potential, both $O_w \cdots H - O_C$ and $O_w - H \cdots O_C$ structures have their existing potential conditions; in our model, a potential more negative than about -0.6 V is needed (-0.6 V is not an exact threshold) to prevent COH* hydrogen returns to the water molecule; similarly, the H_3O^+ structure is stabilized under a potential more positive than -1.2 V. That is to say, the COH* reaction path we described here only exists in the range of about -1.2 V to -0.6 V. Figure 3 shows the optimized structures of IS, TS, and FS of the COH* reaction path under the potential of -0.8 V.

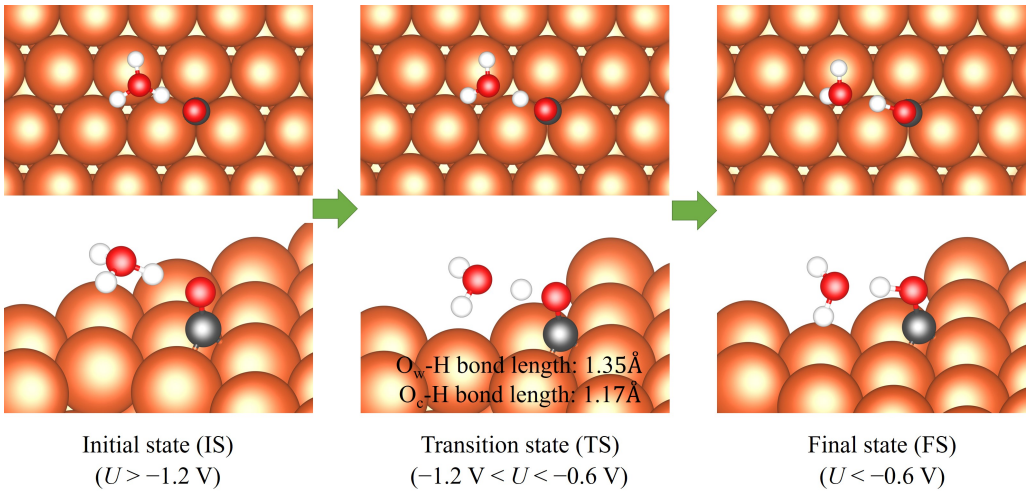

Figure 3. Top and side view of the optimized structure of IS, TS, and FS of the elementary step of CO* reduction to COH* intermediate under the potential of -0.8 V (orange = copper, red = oxygen, gray = carbon, white = hydrogen).

Figure 4a shows energies of structures along the MEP of CO* reduction to COH* from -0.8 V to -1.0 V. The activation barrier for this reaction path is quite low and goes lower when a more negative potential is applied. The result for -1.0 V are close to a non-barrier process, which means the IS of the reaction path will no longer exist and the reaction will

proceed spontaneously once a H_3O^+ species approaches the CO* at a potential lower than −1.0 V. On the other hand, when the potential is higher, the COH* intermediate will never come to the formation, as we mentioned before.

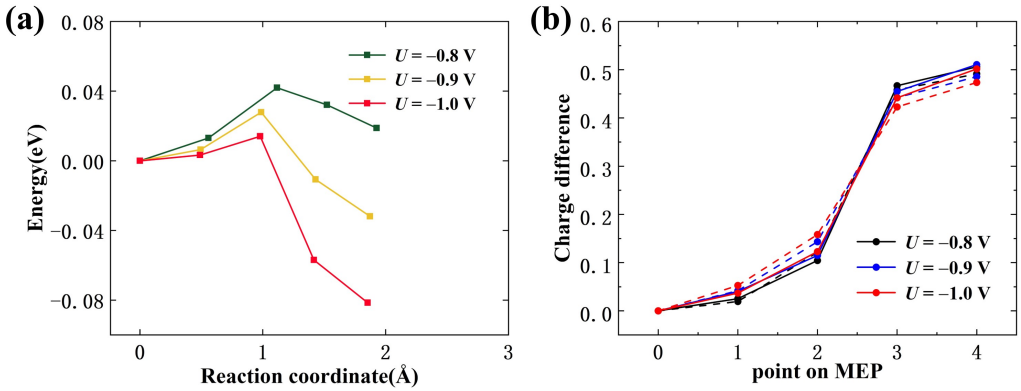

Figure 4. (**a**) Energies of structures and (**b**) changes of system charge (dashed lines) and adsorbed species Bader charge (solid lines) along the MEP of CO* reduction to COH* from −0.8 V to −1.0 V.

The barrier between the IS and FS is quite interesting. At first, we thought the barrier was caused by the transition of the proton from the water molecule to the CO molecule; however, the vibration mode of the imaginary frequency of the TS is not the H stretching vibration, but the orientation twisting of the water molecule (see Supplementary Materials for details), which means the barrier is actually caused by the orientation change of the water molecule (and the orientation change of the water molecule is due to the charged surface), thus the COH* path has no truly TS. This result is consistent with the study of Zhao et al. in 2021 [14], as they calculated the COH* formation via Proton-Coupled Electron Transfer (PCET) pathway and find that no transition state observed, which means the bond break between the water molecule and the proton (or between the CO molecule and the proton, from the other side of the reaction) needs no activation energy in this reaction. This phenomenon may be due to the presence of hydrogen bonds.

The activation barrier and reaction energy obviously varies with the potential due to the significant system charge difference along the reaction. Figure 4b shows that the charge of adsorbed species changes almost synchronously with the system charge, and about 0.5 e charge was transferred during the reaction.

The Bader charge analysis (listed in Table 2) shows that the reduction of CO* to COH* needs about 0.28 e of charge, and the charge of the transferred hydrogen atom does not change much and remains around 0.7 e, as we can see in the Table 2. Such a hydrogen atom could be regarded as a proton. Then, we can describe the whole process clearly as the formation of the O-H bond on CO* via proton transfer, accompanied by charge transfer from the electrode to the adsorbed species, which can be written as $CO^* + H^{x+} + xe^- \longrightarrow COH^*$.

Table 2. Bader charge analysis on key fragments at each point on the MEP of COH* path at various potentials.

Potential	Atom or Fragment	Structures along the MEP				
		0	1	2	3	4
−0.8 V	Cu [1]	0.268	0.261	0.271	0.277	0.281
	C	0.403	0.405	0.449	0.249	0.225
	O	−1.057	−1.069	−1.137	−1.177	−1.152
	H	0.713	0.706	0.685	0.670	0.656
	H_2O	0.196	0.188	0.154	0.047	0.020

Table 2. *Cont.*

Potential	Atom or Fragment	Structures along the MEP				
		0	**1**	**2**	**3**	**4**
−0.9 V	Cu	0.271	0.267	0.278	0.283	0.279
	C	0.389	0.444	0.417	0.250	0.210
	O	−1.064	−1.140	−1.142	−1.188	−1.182
	H	0.701	0.692	0.679	0.663	0.680
	H_2O	0.202	0.192	0.104	0.056	0.009
−1.0 V	Cu	0.273	0.264	0.262	0.268	0.274
	C	0.367	0.365	0.380	0.246	0.198
	O	−1.072	−1.087	−1.138	−1.203	−1.198
	H	0.707	0.680	0.671	0.665	0.686
	H_2O	0.185	0.193	0.151	0.037	−0.001

[1] Cu represent the three Cu atoms whose hollow site is absorbed by C atom.

2.3. CO Poisoning

It is necessary to investigate CO poisoning at different potentials. In order to describe the binding strength between CO and copper atoms, we calculated a crystal orbital Hamilton population (COHP). The projected density of state (pDOS) and projected COHP (pCOHP) of a Cu(111) slab with a CO adsorbate at the potential of 0.0 V are shown in Figure 5.

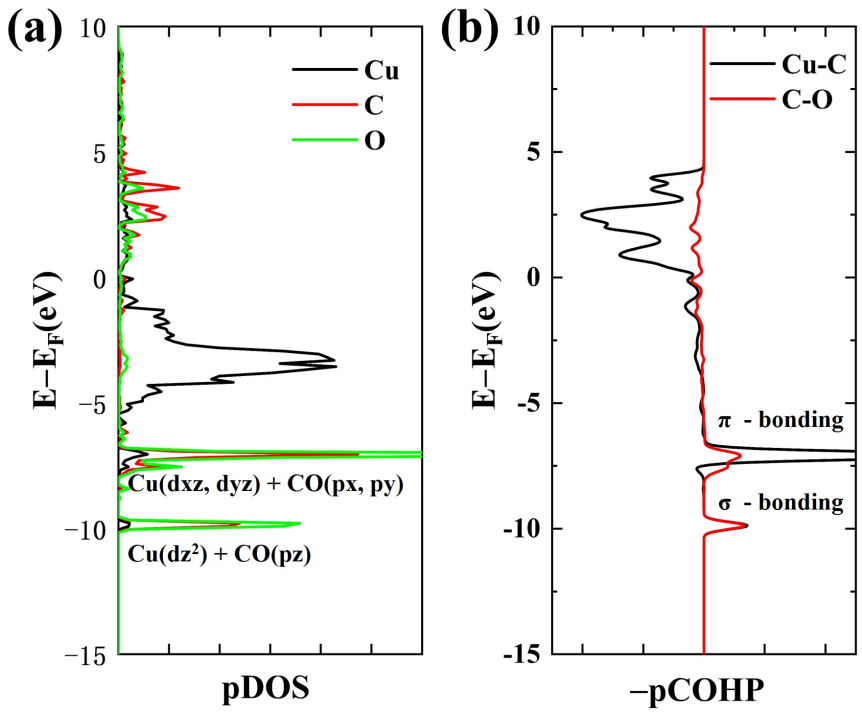

Figure 5. (**a**) pDOS and (**b**) −pCOHP of Cu(111) slab with a CO adsorbate at the potential of 0.0 V.

Then, we calculated ICOHP (integrated COHP to Fermi level) at different potentials and different CO coverage (Figure 6a, different CO coverage structures are provided in Supplementary Materials, Figure S2). It can be seen from Figure 6a that the binding strength of CO decreases when the CO coverage goes higher, which shows that Cu(111) surfaces are not easy to be poisoned by CO. Additionally, different CO coverage structures have different responses to the variation of potential, high CO coverage structures have stronger CO binding strength as the potential becomes lower, but structures with low CO coverage have a smaller tendency. We know that during the process of CO adsorption on the copper surface, the copper atom donates electrons to $\sigma - \pi$ bond between Cu and C.

As the negative potential is applied, the copper surface becomes more inclined to provide electrons; thus, the bonding will become stronger. One speculation as to the cause of the behavior of low CO coverage structures may be due to the shift of the d-band center of copper. As we can see in Figure 6b, the d-band center of the copper surface has been lowered when the potential increases, and a lower d-band center caused weaker Cu-C bonding and low CO coverage structure may be more sensitive to the effect of d-band center shift.

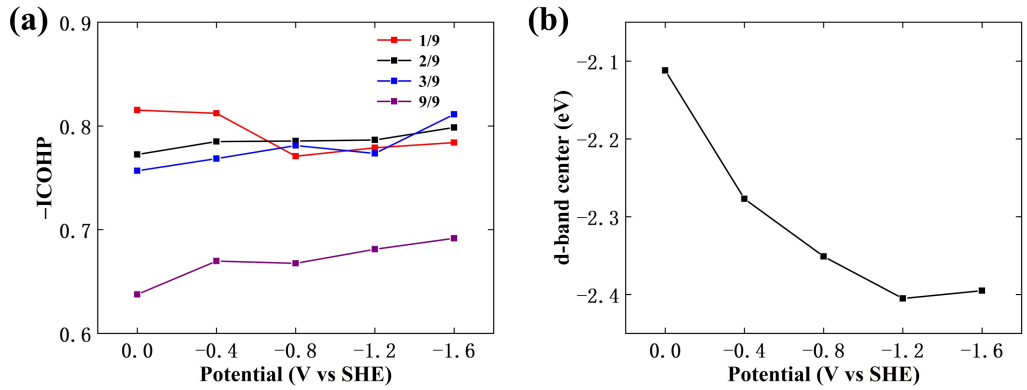

Figure 6. (**a**) −ICOHP at different potentials and different CO coverage. (**b**) d-band center of surface Cu atoms at different potentials.

3. Computational Methods

3.1. Constant Potential Model

Here we describe the constant potential model developed by Duan et al. [12] in brief. In a constant potential system, the number of electrons were changed during atomic structural changes, such a system can be treated as a grand canonical system. The corrected energy of the grand canonical system (H) that considers both atomic positions ($\mathbf{r}$) and number of electron s(n) as variables can be written as:

$$H(\mathbf{r}, n) = E(\mathbf{r}, n) - (n - n_0)\phi \tag{1}$$

where E is the internal potential energy, $\mathbf{r}$ is the Cartesian coordinates, n_0 is the total number of nuclear charges, and ϕ is the effective energy level of the counter electrode. The relation between ϕ and the applied voltage U when taking the standard hydrogen electrode (SHE) as the reference electrode is:

$$\phi = -4.44\ \mathrm{V} - U \tag{2}$$

we determined the absolute potential of the SHE to be 4.44 V according to experiments [15,16]. The electron chemical potential then can be written as:

$$\mu = \frac{\partial E}{\partial n} - \phi = E_f/e - \phi \tag{3}$$

where E_f is the Fermi level of the electrode which we are concerned with, and can be obtained from DFT calculations.

The full gradient of $H(\mathbf{r}, n)$ is then $(\partial H/\partial \mathbf{r}, \partial H/\partial n) = (-\mathbf{f}, \mu)$. Geometry optimization and saddle point search under constant potential can then be performed using this gradient combined with optimization algorithms. In an eNEB run, in addition to the given initial guess of the geometric structure, the initial guess of the number of electrons in the system is also needed. The number of electrons, as with the geometric structure, is also obtained through self-consistent calculations. More details and the program package can be found in Ref. [12].

3.2. Electronic Structure Methods

A periodic slab model was used to describe catalyst surfaces. We constructed a supercell containing four layers of 3×3 Cu atoms with the bottom 2 layers fixed to simulate the bulk properties. A vacuum space of 15 Å thickness along the z-axis was set to avoid interactions between surface adsorbed species and the lower surface of another periodic structure above.

All electronic structure calculations in this paper were performed in the Vienna Ab-initio Simulation Package (VASP) [17,18] within the framework of DFT. The plane wave pseudopotential basis set was used in calculations, and the cutoff energy of the plane wave basis set was set to 400 eV (The results of the convergence test of the cutoff energy are provided in the Supplementary Materials, Table S1). A $3 \times 3 \times 1$ Gamma-centered k-point mesh was used to sample the Brillouin region. Electronic exchange and correlation were described using the Perdew–Burke–Ernzerhof (PBE) functional [19], and the threshold for electronic energy in SCF iteration was set to 1×10^{-6} eV. Since the system we are concerned with is an open shell structure, spin polarization is considered. We describe the weak interactions such as hydrogen bonds by the Grimme DFT-D3 dispersion correction method [20]. The solvent environment of the system is described by an implicit solvent model implemented in the VASPsol program [21–23] by Hennig's group. In the implicit solvent model, the relative permittivity was set to 80 to simulate the aqueous environment. Geometry optimization calculations proceeded under constant potential, transition states were located using a climbing image-nudged elastic band (CI-NEB) method combined with the constant potential algorithm, as implemented in the eNEB code [12]. The local minimum and transition state structures were fully relaxed under constant potentials until the maximum atomic force was less than 0.05 eV/Å. All transition states were confirmed by frequency calculations, and the imaginary frequencies and vibration modes are provided in Supplementary Materials. The MEP curves are plotted using energies vs. reaction coordinates, each reaction coordinate corresponds to the relative position of each atom in a given reaction system, thus the specific form of reaction coordinates depends on the motion trajectory of atoms along the MEP. The energies we use here were corrected by adding $-(n - n_0)V_{sol}$ to the corrected energy in Equation (1) to remove the interaction between the charged system and its compensating charge, which is actually nonexistent. Bader charge analysis was finished by the program package developed by Henkelman's group [24–27], and COHP calculation was done using Lobster program [28,29].

4. Conclusions

We performed a detailed mechanistic study of the two competing reactions for the Cu(111) catalyzed electroreduction, the formation of *CHO intermediate and the formation of *COH intermediate, via a constant potential model, taking charge effects and solvent effects into account.

We found that the elementary step of CO* forming CHO* intermediate through surface hydrogen H* transfer, which was previously considered to be a non-electrochemical and potential-independent process, actually involved partial charge transfer and have potential dependence on the activation barrier and reaction energy.

We explored the elementary step of CO* reduction to COH* intermediate, confirming that this path exists only in a specific potential interval. This process involves significant charge transfer, thus the activation energy barrier and the reaction energy are greatly affected by potential changes.

Comparing the reaction paths of these two intermediates, we infer that the first step of reduction of CO* favors the formation of CHO* at high potentials and COH* at lower potentials. The instability of COH* intermediates at high potentials may be able to explain the relatively negative production potential of methane in Cu catalyzed CO_2 electroreduction experiments [2].

We investigated the CO poisoning on a Cu surface. It is found that the binding strength between CO and copper atoms decreases when the CO coverage goes higher. CO binds

stronger on the Cu surface when the potential goes lower because of more electron donation to the Cu-C bond, but this trend is smaller for low CO coverage structures, possibly due to greater sensitivity to the effect of d-band center shift.

Supplementary Materials: The following supporting information can be downloaded at: https://www.mdpi.com/article/10.3390/catal13060960/s1, Table S1: The convergence test of the cutoff energy of the plane wave basis set; Table S2: The imaginary frequencies of the TSs; Figure S1: The vibration mode of the imaginary frequencies; Figure S2: Different CO coverage structures.

Author Contributions: Conceptualization, S.M.; methodology, S.M.; software, W.L.; validation, S.M. and W.L.; formal analysis, S.M.; investigation, S.M.; resources, W.L.; data curation, S.M.; writing—original draft preparation, S.M.; writing—review and editing, S.M. and W.L.; visualization, S.M.; supervision, W.L.; project administration, S.M.; funding acquisition, W.L. All authors have read and agreed to the published version of the manuscript.

Funding: This research was funded by National Natural Science Foundation of China (grant number 21833006 and 22173074).

Data Availability Statement: Not applicable.

Acknowledgments: The support of State Key Laboratory of Physical Chemistry of Solid Surfaces, Fujian Provincial Key Laboratory of Theoretical and Computational Chemistry, College of Chemistry and Chemical Engineering of Xiamen University of China is acknowledged.

Conflicts of Interest: The authors declare no conflict of interest.

References

1. Olah, G.A.; Prakash, G.S.; Goeppert, A. Anthropogenic chemical carbon cycle for a sustainable future. *J. Am. Chem. Soc.* **2011**, *133*, 12881–12898. [CrossRef] [PubMed]
2. Hori, Y.; Murata, A.; Takahashi, R. Formation of hydrocarbons in the electrochemical reduction of carbon dioxide at a copper electrode in aqueous solution. *J. Chem. Soc. Faraday Trans. 1 Phys. Chem. Condens. Phases* **1989**, *85*, 2309–2326. [CrossRef]
3. Hori, Y.; Takahashi, R.; Yoshinami, Y.; Murata, A. Electrochemical reduction of CO at a copper electrode. *J. Phys. Chem. B* **1997**, *101*, 7075–7081. [CrossRef]
4. Hori, Y.I. Electrochemical CO_2 reduction on metal electrodes. In *Modern Aspects of Electrochemistry*; Springer: Berlin/Heidelberg, Germany, 2008; pp. 89–189.
5. Bagger, A.; Ju, W.; Varela, A.S.; Strasser, P.; Rossmeisl, J. Electrochemical CO_2 reduction: A classification problem. *ChemPhysChem* **2017**, *18*, 3266–3273. [CrossRef] [PubMed]
6. Peterson, A.A.; Abild-Pedersen, F.; Studt, F.; Rossmeisl, J.; Nørskov, J.K. How copper catalyzes the electroreduction of carbon dioxide into hydrocarbon fuels. *Energy Environ. Sci.* **2010**, *3*, 1311–1315. [CrossRef]
7. Nie, X.; Esopi, M.R.; Janik, M.J.; Asthagiri, A. Selectivity of CO_2 reduction on copper electrodes: The role of the kinetics of elementary steps. *Angew. Chem.* **2013**, *125*, 2519–2522. [CrossRef]
8. Zhao, Q.; Carter, E.A. Revisiting competing paths in electrochemical CO_2 reduction on copper via embedded correlated wavefunction theory. *J. Chem. Theory Comput.* **2020**, *16*, 6528–6538. [CrossRef]
9. Xiao, H.; Cheng, T.; Goddard, W.A., III; Sundararaman, R. Mechanistic explanation of the pH dependence and onset potentials for hydrocarbon products from electrochemical reduction of CO on Cu (111). *J. Am. Chem. Soc.* **2016**, *138*, 483–486. [CrossRef]
10. Sundararaman, R.; Goddard, W.A., III; Arias, T.A. Grand canonical electronic density-functional theory: Algorithms and applications to electrochemistry. *J. Chem. Phys.* **2017**, *146*, 114104. [CrossRef]
11. Taylor, C.D.; Wasileski, S.A.; Filhol, J.S.; Neurock, M. First principles reaction modeling of the electrochemical interface: Consideration and calculation of a tunable surface potential from atomic and electronic structure. *Phys. Rev. B* **2006**, *73*, 165402. [CrossRef]
12. Duan, Z.; Xiao, P. Simulation of Potential-Dependent Activation Energies in Electrocatalysis: Mechanism of O–O Bond Formation on RuO2. *J. Phys. Chem. C* **2021**, *125*, 15243–15250. [CrossRef]
13. Nie, X.; Luo, W.; Janik, M.J.; Asthagiri, A. Reaction mechanisms of CO_2 electrochemical reduction on Cu (111) determined with density functional theory. *J. Catal.* **2014**, *312*, 108–122. [CrossRef]
14. Zhao, Q.; Martirez, J.M.P.; Carter, E.A. Revisiting understanding of electrochemical CO_2 reduction on Cu (111): Competing proton-coupled electron transfer reaction mechanisms revealed by embedded correlated wavefunction theory. *J. Am. Chem. Soc.* **2021**, *143*, 6152–6164. [CrossRef]
15. Trasatti, S. Structure of the metal/electrolyte solution interface: New data for theory. *Electrochim. Acta* **1991**, *36*, 1659–1667. [CrossRef]

16. Donald, W.; Leib, R.; O'Brien, J.; Williams, E. Directly Relating Gas-Phase Cluster Measurements to Solution-Phase Hydrolysis, the Absolute Standard Hydrogen Electrode Potential, and the Absolute Proton Solvation Energy. *Chem. Eur. J.* **2010**, *15*, 5926–5934. [CrossRef] [PubMed]
17. Kresse, G.; Furthmüller, J. Efficiency of ab-initio total energy calculations for metals and semiconductors using a plane-wave basis set. *Comput. Mater. Sci.* **1996**, *6*, 15–50. [CrossRef]
18. Kresse, G.; Furthmüller, J. Efficient iterative schemes for ab initio total-energy calculations using a plane-wave basis set. *Phys. Rev. B* **1996**, *54*, 11169. [CrossRef]
19. Perdew, J.P.; Burke, K.; Ernzerhof, M. Generalized gradient approximation made simple. *Phys. Rev. Lett.* **1996**, *77*, 3865. [CrossRef]
20. Grimme, S.; Antony, J.; Ehrlich, S.; Krieg, H. A consistent and accurate ab initio parametrization of density functional dispersion correction (DFT-D) for the 94 elements H-Pu. *J. Chem. Phys.* **2010**, *132*, 154104. [CrossRef]
21. Mathew, K.; Kolluru, V.S.C.; Hennig, R.G. VASPsol: Implicit Solvation and Electrolyte Model for Density-Functional Theory. 2018. Available online: https://github.com/henniggroup/VASPsol (accessed on 9 July 2022).
22. Mathew, K.; Sundararaman, R.; Letchworth-Weaver, K.; Arias, T.; Hennig, R.G. Implicit solvation model for density-functional study of nanocrystal surfaces and reaction pathways. *J. Chem. Phys.* **2014**, *140*, 084106. [CrossRef]
23. Mathew, K.; Kolluru, V.C.; Mula, S.; Steinmann, S.N.; Hennig, R.G. Implicit self-consistent electrolyte model in plane-wave density-functional theory. *J. Chem. Phys.* **2019**, *151*, 234101. [CrossRef] [PubMed]
24. Tang, W.; Sanville, E.; Henkelman, G. A grid-based Bader analysis algorithm without lattice bias. *J. Phys. Condens. Matter* **2009**, *21*, 084204. [CrossRef] [PubMed]
25. Sanville, E.; Kenny, S.D.; Smith, R.; Henkelman, G. Improved grid-based algorithm for Bader charge allocation. *J. Comput. Chem.* **2007**, *28*, 899–908. [CrossRef] [PubMed]
26. Henkelman, G.; Arnaldsson, A.; Jónsson, H. A fast and robust algorithm for Bader decomposition of charge density. *Comput. Mater. Sci.* **2006**, *36*, 354–360. [CrossRef]
27. Yu, M.; Trinkle, D.R. Accurate and efficient algorithm for Bader charge integration. *J. Chem. Phys.* **2011**, *134*, 064111. [CrossRef]
28. Dronskowski, R.; Bloechl, P.E. Crystal orbital Hamilton populations (COHP): Energy-resolved visualization of chemical bonding in solids based on density-functional calculations. *J. Phys. Chem.* **1993**, *97*, 8617–8624. [CrossRef]
29. Deringer, V.L.; Tchougréeff, A.L.; Dronskowski, R. Crystal orbital Hamilton population (COHP) analysis as projected from plane-wave basis sets. *J. Phys. Chem. A* **2011**, *115*, 5461–5466. [CrossRef]

Disclaimer/Publisher's Note: The statements, opinions and data contained in all publications are solely those of the individual author(s) and contributor(s) and not of MDPI and/or the editor(s). MDPI and/or the editor(s) disclaim responsibility for any injury to people or property resulting from any ideas, methods, instructions or products referred to in the content.